AMERICAN SOCIETY FOR MICROBIOLOGY | Applied and Environmental Microbiology

Molecular and Cellular Biology | Full-Length Text

Quantitative morphological analysis of *Deinococcus radiodurans* elucidates complex dose-dependent nucleoid condensation during recovery from ionizing radiation

Antonio Cordova,[1,2] Brandon Niese,[3] Philip Sweet,[1] Pratik Kamat,[4] Jude M. Phillip,[4,5] Vernita Gordon,[2,3,6] Lydia M. Contreras[2,7]

AUTHOR AFFILIATIONS See affiliation list on p. 21.

ABSTRACT The extremophile *Deinococcus radiodurans* maintains a highly organized and condensed nucleoid as its default state, possibly contributing to its high tolerance to ionizing radiation (IR). Previous studies of the *D. radiodurans* nucleoid were limited by reliance on manual image annotation and qualitative metrics. Here, we introduce a high-throughput approach to quantify the geometric properties of cells and nucleoids using confocal microscopy, digital reconstructions of cells, and computational modeling. We utilize this novel approach to investigate the dynamic process of nucleoid condensation in response to IR stress. Our quantitative analysis reveals that at the population level, exposure to IR induced nucleoid compaction and decreased the size of *D. radiodurans* cells. Morphological analysis and clustering identified six distinct sub-populations across all tested experimental conditions. Results indicate that exposure to IR induced fractional redistributions of cells across sub-populations to exhibit morphologies associated with greater nucleoid condensation and decreased the abundance of sub-populations associated with cell division. Nucleoid-associated proteins (NAPs) may link nucleoid compaction and stress tolerance, but their roles in regulating compaction in *D. radiodurans* are unknown. Imaging of genomic mutants of known and suspected NAPs that contribute to nucleoid condensation found that deletion of nucleic acid-binding proteins, not previously described as NAPs, can remodel the nucleoid by driving condensation or decondensation in the absence of stress and that IR increased the abundance of these morphological states. Thus, our integrated analysis introduces a new methodology for studying environmental influences on bacterial nucleoids and provides an opportunity to further investigate potential regulators of nucleoid condensation.

IMPORTANCE *Deinococcus radiodurans*, an extremophile known for its stress tolerance, constitutively maintains a highly condensed nucleoid. Qualitative studies have described nucleoid behavior under a variety of conditions. However, a lack of quantitative data regarding nucleoid organization and dynamics has limited our understanding of the regulatory mechanisms controlling nucleoid organization in *D. radiodurans*. Here, we introduce a quantitative approach that enables high-throughput quantitative measurements of subcellular spatial characteristics in bacterial cells. Applying this to wild-type or single-protein-deficient populations of *D. radiodurans* subjected to ionizing radiation, we identified significant stress-responsive changes in cell shape, nucleoid organization, and morphology. These findings highlight this methodology's adaptability and capacity for quantitatively analyzing the cellular response to stressors for screening cellular proteins involved in bacterial nucleoid organization.

KEYWORDS DNA condensation, nucleoid-associated proteins, confocal microscopy, ionizing radiation

Editor Haruyuki Atomi, Kyoto University, Kyoto, Japan

Address correspondence to Lydia M. Contreras, lcontrer@che.utexas.edu.

Antonio Cordova and Brandon Niese contributed equally to this article. Author order was determined by placement in alphabetical order.

The authors declare no conflict of interest.

See the funding table on p. 21.

Received 20 January 2024
Accepted 19 May 2024
Published 12 June 2024

The compaction of the chromosome into a hierarchically organized irregularly shaped nucleoid is one example of subcellular spatial organization in bacteria (1, 2). Nucleoids contain all or most of the genetic materials of the bacterial cell and are essential to gene expression and cell division (1). Regulation of the structural organization and the morphologies of bacterial nucleoids are best understood only in a few model organisms, such as *Escherichia coli* and *Bacillus subtilis* (3). Furthermore, molecular mechanisms that explain the dynamics of how nucleoids change shapes under different cellular and environmental conditions are not well understood, particularly in the context of stress-response regulation.

Since genomic material requires compaction to fit into the cell, it has been proposed that multiple classes of cellular factors and mechanisms are involved in forming the bacterial nucleoid. These classes include nucleoid-binding proteins, non-coding nucleoid-associated RNAs (4), and DNA supercoiling mechanisms (5). Nucleoid-associated proteins (NAPs) are suspected to contribute to DNA-DNA contacts that promote higher-order organization. For example, the *E. coli* NAP, histone-like nucleoid structuring protein, and *B. subtilis* NAPs, ParB and structural maintenance of chromosomes, facilitate DNA bridging and higher-order organization (6). Likewise, histone-like protein (HU) binds to and bends DNA to maintain the nucleoid (7). In addition to protein factors, a study of *E. coli* has identified the presence of a noncoding RNA (naRNA4) in the nucleoid fraction; it has been suggested that naRNA4 may, in association with nucleoid-associated proteins (like HU), contribute to DNA compaction by forming more remote DNA-DNA connections (8).

In addition to providing structure to the nucleoid, NAPs can contribute to stress tolerance. For example, HU homologs in extremophilic bacteria are suspected to play a role in survival under radiation-based stressors (9), and the *E. coli* Dps protein, which protects DNA from oxidative damage, also contributes to DNA condensation (10, 11).

Earlier *E. coli* studies have shown that the nucleoid structure is dynamic and responsive to both changes in the physiological state of the cell (2) and to changes in environmental conditions (12). For instance, oxidative stress that threatens DNA integrity has been shown to induce nucleoid compaction (13). In *B. subtilis*, a qualitative study found that under non-stressed conditions, the nucleoid occupied most of the cell volume and that non-lethal exposures to UV light resulted in compacted chromosomes and elongated cells (14). This change in nucleoid morphology is reversible, particularly after lower doses of UV, in a way that depends on active mechanisms of DNA repair. These findings suggest that this case of nucleoid compaction might be correlated with active and controlled DNA repair and/or to mechanisms of DNA protection under stress. For instance, in *E. coli*, RecA is a key protein associated with DNA repair, and the association of DNA with the active form of RecA affects nucleoid compaction (12). In similar studies, damage to DNA and/or disruptions to DNA repair induced in *Mycobacterium smegmatis* (15) and *Staphylococcus aureus* (13) also led to compaction of the genome. Specifically, studies on DNA damage stress in *E. coli* found the bacterial chromatin compacted down to fill ~20% of the cell volume when exposed to nalidixic acid, a double-strand DNA damage agent, as opposed to occupying the majority of the cytoplasmic, ribosome-free space, under no stress (12). In summary, many studies across many organisms have suggested that the volume fraction of the cell occupied by the nucleoid and how the nucleoid reconfigures after stress are both of biological relevance.

Ionizing radiation (IR) contributes to cellular stress in bacteria as a complex environmental condition capable of introducing direct damage to DNA (16) and indirect cellular damage via oxidative stress (17, 18). In most bacteria, including *E. coli* and *B. subtilis,* the D_{10} value (the dose of ionizing radiation required to reduce a bacterial population to 10% of its initial size) is less than 1 kGy (19). In stark contrast, the stress-resistant extremophile *Deinococcus radiodurans* has a uniquely high radiation tolerance (D_{10} value of ~12.5 kGy) (20). Characteristics that have been suggested as possibly contributing to *D. radiodurans*' tolerance of oxidative stressors, such as IR, include its robust DNA repair machinery, the signal recognition particle pathway of antioxidant protein transport,

its IR-sensitive post-transcriptional regulator network, and its constitutively compacted genome (21–27). The last is of particular importance for the work we present here.

Examining the nucleoid structure and dynamics in an organism, like *D. radiodurans*, that maintains a highly organized and complex condensed nucleoid by default has the potential to shed light on how subcellular organization is regulated under IR (28). The multifaceted genome content of *D. radiodurans* comprises two chromosomes, [Chr I (2,648,638 bp) and Chr II (412,348 bp)], a megaplasmid (177,466 bp), and a plasmid (45,704 bp) (29). Moreover, *D. radiodurans* maintains multiplicate copies of its genome content, which can vary between growth phases (8–10 in exponential growth and 4 in stationary growth) (30, 31). Understanding how the organization and response dynamics of the condensed *D. radiodurans* nucleoid contribute to its high IR tolerance and how this depends on the activity of DNA-binding proteins and nucleoid-associated proteins has the potential to provide a unique perspective on subcellular organization in prokaryotes.

Qualitative studies of *D. radiodurans* (28, 32–34) have confirmed that nucleoid morphology is highly dynamic during the cell cycle, even in the absence of any environmental stresses. Prior qualitative descriptions of the *D. radiodurans* nucleoid under stress have been based on fluorescent microscopy and cryo-electron microscopy (33, 34). These earlier, qualitative studies point to the need for deeper investigation of the dynamics of nucleoids. Deeper investigation requires methods for quantitative image analysis with the ability to measure many types of geometric properties that can be defined by investigators *ad hoc* to better map the dynamics of nucleoids. Ideally, such an approach would also be high-throughput, able to quickly analyze large numbers of cells as well as many different geometric parameters.

Here, we develop a method for the quantitative measurement of the geometric properties of bacterial cells and nucleoids. We applied this method to populations of *Deinococcus radiodurans* to study the impact of IR and the contributions of different nucleic acid-binding proteins on nucleoid structure. Our approach used machine learning to create analyzable digital re-creations of individual bacterial cells from laser-scanning confocal microscopy images of cells pre- and post-IR exposure. Digital re-creations were input into Python code for analysis so that any user-defined parameter can be measured. Following either IR exposure or the deletion of genes encoding for single proteins, we measured statistically significant changes in spatial and geometric parameters of *D. radiodurans*. Consistent with previous observations of bacteria under DNA-damaging stress, we found that exposure to IR results in decreased cell area while also resulting in more circular, less eccentric nucleoids. Our quantitative method also allowed us to measure previously unreported shifts in the nucleoid area and the fraction of the cell occupied by the nucleoid. We tracked these dose-dependent geometric parameters over 18 hours to measure the dynamics of recovery after exposure to IR and we showed that the recovery process also varies with initial, acute dose.

In tandem with our quantitative method, our morphological clustering analysis identified extremes in cell and nucleoid morphology that can effectively assist in determining bacterial sub-populations across experimental conditions. We found that exposure to IR decreased the representation of sub-populations with morphological features associated with cell division. Additionally, we found that IR stress increased the representation of sub-populations with morphologies associated with greater nucleoid condensation. We found that the representation of these morphological clusters can be driven by the deletion of specific proteins in *D. radiodurans,* which we hypothesize contributes to the mechanisms of nucleoid dynamics under stress. Specifically, we identified DNA-binding, RNA-binding, and stress-response proteins that were not previously identified as nucleoid-associated to have significant effects on nucleoid remodeling under sham (no radiation) conditions when their encoding genes are deleted. We also observed that sub-populations, representative of morphological states of nucleoid condensation or decondensation in the absence of stress, were significantly increased when cells were exposed to IR. Collectively, our results indicated that this approach can be used to screen candidate proteins for their role in IR tolerance and

recovery. Overall, this integrated analysis introduces a novel approach for measuring changes in cell and nucleoid geometry and for the investigation of key genes, known or unknown, in nucleoid condensation.

RESULTS

Confocal laser-scanning microscopy enables qualitative capture of the characteristics of *D. radiodurans* nucleoids

To establish quantitative measures for the geometric properties of *D. radiodurans* cells and nucleoids, we first characterized a wild-type strain (R1) in the presence and absence of ionizing radiation. The experimental scheme we used is illustrated in Fig. 1A and described in more detail in Materials and Methods. In brief, bacterial cultures were exposed to different doses of ionizing radiation (0–12 kGy); 12 kGy was selected because *D. radiodurans* has a D_{10} value of ~12.5 kGy (35). Following irradiation and a 2-hour recovery period at 30°C, cells were stained with two fluorescent dyes, Nile Red and Syto 9 Green, which associate with the hydrophobic region of the bacterial cell membrane and the bacterial DNA, respectively. The two dyes Nile Red and Syto 9 Green have two different spectra for fluorescence excitation and emission, allowing the cell membrane (red) and the nucleoid (green) to be differentiated by color. We used laser-scanning confocal microscopy to image stained bacteria in these two separate image channels (Fig. 1B).

Characterization of *D. radiodurans* survival and recovery after irradiation was performed by counting colony-forming units (CFU) and reporting the survival fraction and by quantifying optical density over time to measure growth (Fig. S1A and B). Our data confirmed a decrease in viable surviving bacteria and a decrease in growth rate with IR exposure doses approaching 10 kGy or greater, as observed in our previous work (25).

In *D. radiodurans* cells that were not exposed to radiation, nucleoids are condensed and irregularly shaped (Fig. 1B) and membranes have a roughly circular cross-section (with flattening where they adjoin other cells in *D. radiodurans*' characteristic tetrad arrangement). These findings, i.e., constitutively condensed nucleoids inside quasi-spherical cells that are arranged in tetrads, are in agreement with published observations about *D. radiodurans*' baseline state in the absence of radiation or other stressors (34).

Importantly, during recovery post-exposure to ionizing radiation, cells trended toward more circular nucleoids as the levels of radiation increased (Fig. 1B). These qualitative trends are consistent with previous reports of more condensed nucleoids in *D. radiodurans* following radiation stress (24).

Development of a quantitative framework for reliably capturing shifts in geometric characteristics of cells

Building on these qualitative observations, we next created a set of quantitative metrics that described the geometric properties of cells and nucleoids and the relationship between both properties. Specifically, we developed a pipeline for quantitative image analysis, beginning with laser-scanning confocal fluorescence images, as shown in Fig. 1B. For every micrograph, both the membrane and the nucleoid grayscale image channels were segmented using the Cellpose (36) machine learning segmentation library. Segmented regions were used to create masks, with each mask showing the fluorescence "footprint" of either one cell membrane or one nucleoid. Using position information, each cell's membrane and nucleoid masks were matched together, with the criterion that there should be only one nucleoid in each cell. A schematic cartoon outlining the key steps of the image analysis pipeline is shown in Fig. 2A.

Defining bulk cell metrics

Five metrics were used to describe the cells: cell area, nucleoid area, nucleoid fractional area (NFA), nucleoid circularity, and nucleoid eccentricity. The area enclosed by the membrane mask was used to measure the cross-sectional area of each cell (cell area),

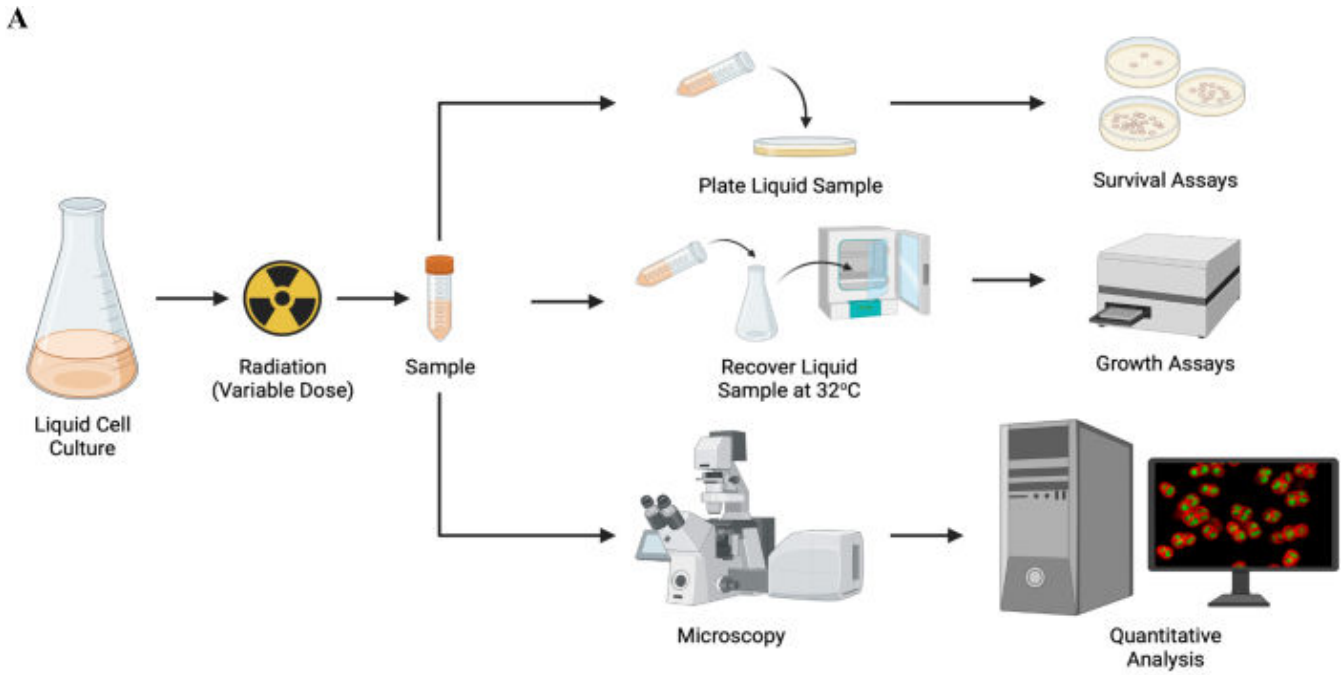

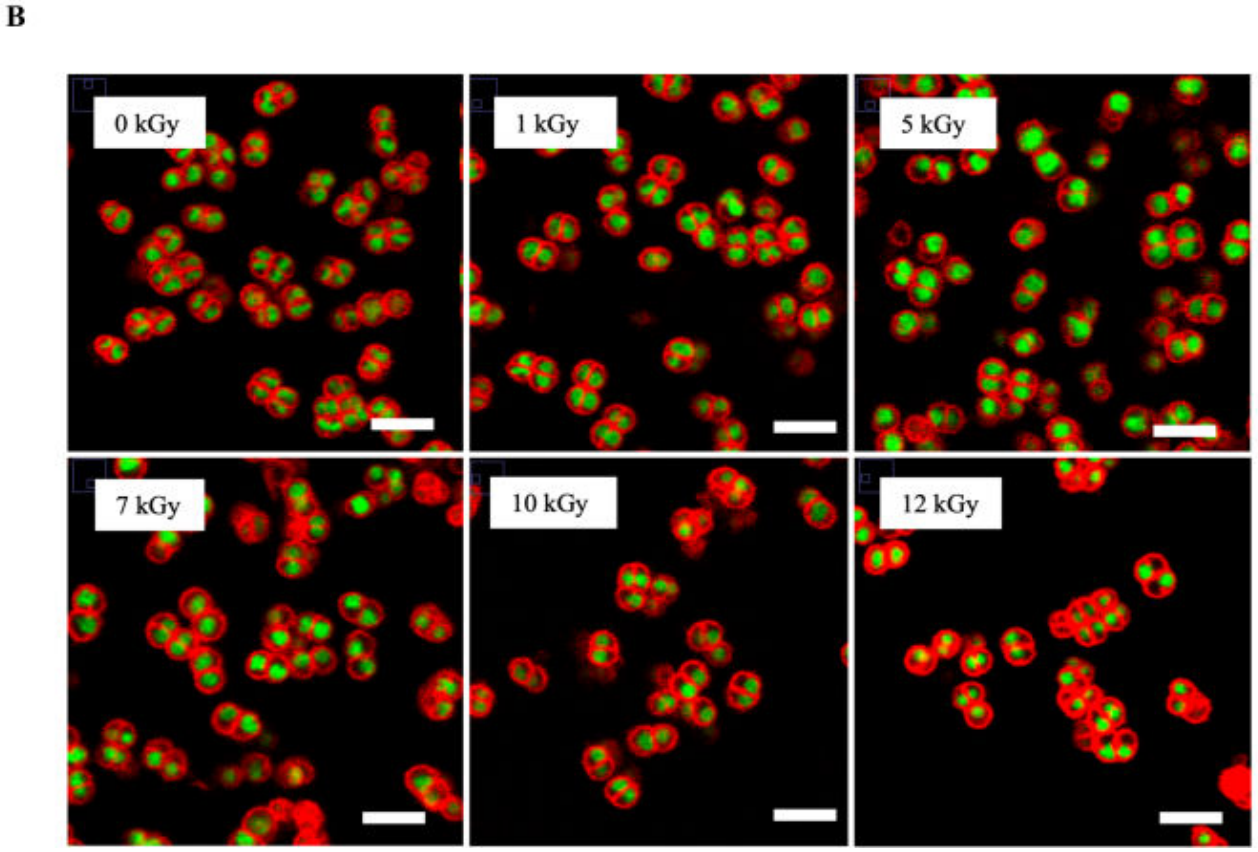

FIG 1 Experiment and analysis scheme, with confocal micrographs to illustrate the raw material for analysis. (A) Experimental scheme. *D. radiodurans* cultures were exposed to IR and then imaged using confocal microscopy. Created in BioRender. (B) Confocal micrographs of wild-type (R1) *D. radiodurans*, with cell membranes stained red and nucleoids stained green. Before imaging, the cells shown were exposed to 0, 1, 5, 7, 10, and 12 kGy radiation, as indicated on subpanels. Scale bars are 5 µm.

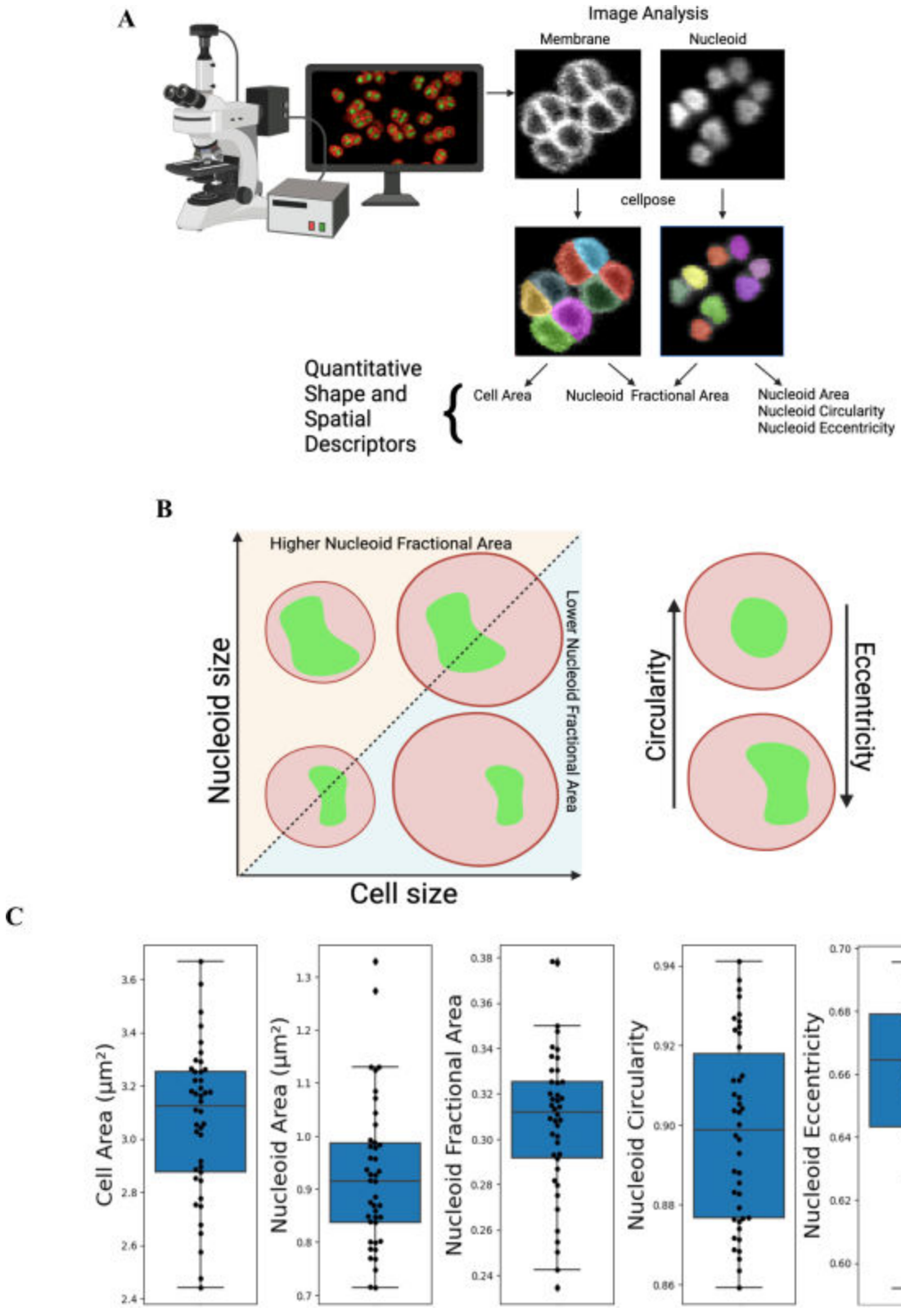

FIG 2 Image analysis for high-throughput quantification of geometric characteristics of cells and nucleoids. (A) The image analysis pipeline begins with laser-scanning confocal fluorescence micrographs, with cell membranes and nucleoids in different image channels. Micrographs are input into Cellpose, which creates segmented binary masks of each cell membrane and each nucleoid. In this figure, distinct binary masks are indicated with different colors. Computational analysis of masks is used to obtain user-defined geometric characteristics. Created in BioRender. (B) The parameter space examined in this study includes

(Continued on next page)

FIG 2 (Continued)

spatial and geometric characteristics. Spatial parameters include cell size, nucleoid size, and nucleoid fractional area. Geometric characteristics include nucleoid circularity and eccentricity. Created in BioRender. (C) Box-and-whisker plots of per-replicate mean values of geometric and spatial parameters for wild-type (R1) *D. radiodurans* cells that have not been irradiated. Means from 24 biological replicate populations are shown (black data points). Boxes show the middle 50% of the means, with horizontal lines representing the median value. Upper/lower whiskers represent upper/lower quartiles. An average of 1,675 cells (min-max 262–3,281) were measured for each biological replicate; 42 biological replicates. For each geometric characteristic measured, probability density distributions are shown in Fig. S2 to S5.

and the area covered by the nucleoid mask was used to measure the cross-sectional area of each nucleoid (nucleoid area). Measuring cell area allows the assessment of spatial changes in cells that are not directly related to any change in nucleoid properties but are likely to arise from radiative damage (37). Since changes in relative cell and nucleoid area sizes are easily conflated with changes in absolute size upon qualitative inspection by the human eye, we provided a quantitative measure of relative cell-nucleoid sizes by introducing the parameter nucleoid fractional area; this is the ratio of nucleoid cross-sectional area to cell cross-sectional area, using the matched pairs of each cell's membrane and nucleoid masks. NFA provided a quantitative measure of the nucleoid size relative to the cell size. A conceptual cartoon of the relationship between cell size, nucleoid size, and nucleoid fractional area is shown in Fig. 2B (left side). In addition to differences in cell and nucleoid size, visual inspection of micrograph images (Fig. 1B) showed differences in the cross-sectional shapes of nucleoids. We measured nucleoid shape using circularity and eccentricity (Fig. 2B).

Using these geometric parameters (the calculations of which are detailed in Materials and Methods), we started by characterizing non-irradiated *D. radiodurans* (Fig. 2C; Fig. S2 to S5). Specifically, we found that, in the absence of radiation stress, wild-type *D. radiodurans* cells had a mean cross-sectional area of about 3 μm^2, and their nucleoids had a mean cross-sectional area of about 0.9 μm^2. Their mean nucleoid fractional area was slightly less than 0.3. The mean nucleoid circularity was about 0.9, and the mean nucleoid eccentricity was about 0.7. Variations across biological replicas across different days were included as empirically measured probability density distributions (Fig. S2 to S5).

Kolmogorov-Smirnov testing (K-S test) was used to determine statistically significant differences associated with irradiation in almost all cases (Fig. S2 to S5; Table S1), as it can compare distributions describing individuals in the entire measured population. K-S tests can exhibit sensitivity to changes in the distribution of a small number of outliers; however, this does not necessarily reflect overall changes in the population.

Bulk quantitative measurements of changes in cellular characteristics during recovery post-exposure to ionizing radiation indicate nucleoid compaction upon radiation exposure

We characterized cell and nucleoid geometries in the wild-type R1 strain, following radiation, and compared these to the geometries measured for the wild-type R1 strain in the absence of radiation. Observed changes in the geometric parameters are shown in Fig. 3A, and the results of significance testing are shown in Table S3. We varied ionizing radiation levels from 0 to 12 kGy. A maximum acute dose of 12 kGy was used to approach the D_{10} value of ~12.5 kGy for *D. radiodurans*. For the measurement of radiation-induced changes while accounting for inter-replicate variation, we recorded the arithmetic mean of each value for the paired irradiated and non-irradiated biological replicates. For each day's replicate, the ratio of the irradiated value to the non-irradiated value measured the fold change in that value. This was recorded for each replicate, for a total of six measurements of fold changes for each characteristic. This normalization approach was intended to account for day-to-day variations, and it parallels day-by-day normalization approaches we have used in previous work (38, 39).

D. radiodurans cells exhibited a statistically significant fold change in both nucleoid fractional area and nucleoid eccentricity following high doses of ionizing radiation.

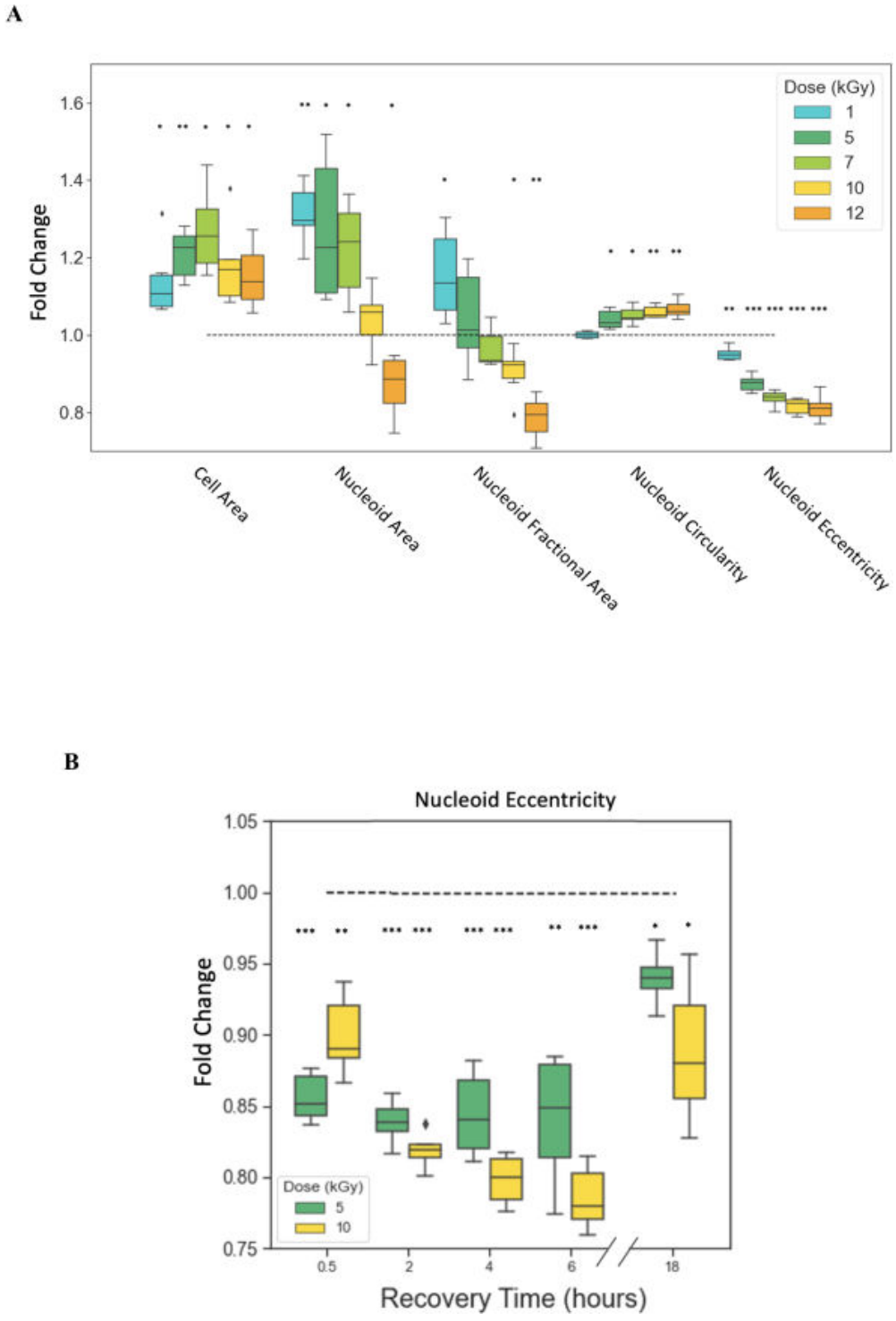

FIG 3 Changes in the geometric characteristics of *D. radiodurans* cells and nucleoids following IR. (A) Fold changes of the mean values of geometric properties from the value measured at 0 kGy. Measured images were taken after 2 hours of recovery. Each box-and-whisker plot contains data from six biological replicates over two experimental days. (B) Fold changes of the mean values of eccentricity from the value measured at 0 kGy for the same biological replicate, at the corresponding recovery time point. Each box-and-whisker plot contains data from six biological replicates over 2 days of experiments. (A and B) *P*-values are calculated using a Student's *t*-test with the null hypothesis that the fold change is equal to 1 (indicated by the black dashed horizontal line). *$P < 0.05$, **$P < 0.001$, and ***$P < 0.0001$.

Nucleoid fractional area decreased, nucleoid circularity increased, and nucleoid eccentricity decreased as radiation doses increased toward 12 kGy (Fig. 3A). The decrease in nucleoid fractional area indicated that the nucleoid is becoming smaller with respect to the cell size. The increase in nucleoid circularity indicated that the nucleoid's perimeter-to-area ratio is decreasing—i.e., it became more condensed. The decrease in eccentricity indicated that the nucleoid had become less elongated. Taken altogether, these observations were consistent with the nucleoid becoming more compact.

Next, we measured the dynamics of *D. radiodurans* cell and nucleoid geometries during recovery from ionizing radiation. We monitored unirradiated and irradiated (5 and 10 kGy) *D. radiodurans* populations for 18 hours after exposure to radiation (Fig. 3B). Cells were imaged at 0.5, 2, 4, 6, and 18 hours after radiation. The initial four time points were chosen to be comparable with the expected doubling time of *D. radiodurans* in our growth conditions (105–130 min) (34, 40). To measure the continued growth of the cell population, we tracked the post-IR optical density (OD_{600}) of the liquid bacterial cultures over the 18-hour period (Fig. S1A). During this period, we found a steady rate of growth following acute IR exposure at 5 and 10 kGy (Fig. S1A). This finding suggests that, despite being exposed to significant levels of ionizing radiation stress, *D. radiodurans* cells were able to continue to grow and divide. However, such growth measurements do not reveal the time course over which cell and nucleoid geometries, having been altered by ionizing radiation, return to the characteristics typifying unirradiated cells.

Next, we explored several important questions, namely, (i) whether all geometric changes observed after irradiation were reversible after a given recovery period, (ii) whether there was a specific time of recovery at which cell and nucleoid changes reverse to pre-radiation geometries, and (iii) whether there was a radiation dose beyond which reversibility in cell and nucleoid changes could not be attained. At each time point during recovery, the fold changes in the geometric properties of each irradiated sample were measured as ratios of the mean measured value (for the irradiated sample) to the corresponding mean values of the non-irradiated (control) population of the same biological replicate at the same time point (Fig. 3B; Fig. S7). The results of significance testing are shown in Table S4. After 18 hours of recovery, the fold change in eccentricity for both populations (5 and 10 kGy) of exposed cells approached 1, a trend which indicated no change relative to the non-irradiated cells, and a return toward the original geometric state of the nucleoid (Fig. 3B). Geometric properties of the *D. radiodurans* cell and nucleoid appeared reversible at 5 kGy and approached 1; however, not all geometric changes observed were reversible after acute IR exposure. We found that recovery after exposure to a 10-kGy IR dose was associated with an irreversible relative fold change in cell area and nucleoid area after 18 hours of recovery following a 10-kGy exposure (Fig. S7).

It is worth noting that there were wide distributions of geometric measurements during the 18-hour recovery period (Fig. S9 to S13), which suggests heterogeneous sub-populations of cells that may not be properly identified in the bulk data analysis.

Cluster analysis of single-cell morphologies reveals consistent enrichment and depletion of sub-populations with exposure to ionizing radiation

Previous studies have manually identified several classes of nucleoid morphologies in unstressed cells (34). This led us to computationally identify subpopulations of cells using clustering algorithms. For this analysis, 32 key morphological parameters, encompassing both nuclear and cellular features, were extracted from approximately 470,000 images of individual cells representing all conditions studied. For this analysis, we used a Cell Profiler pipeline (41) (Table S5). We used a combination of 2D Uniform Manifold Approximation and Projection (UMAP) dimensionality reduction and k-means unsupervised hierarchical clustering to discretize six morphological clusters (Fig. S13) with unique nuclear and cellular morphologies. Importantly, we observed that *D. radiodurans* cells adopted a broad spectrum of morphologies across experimental conditions, with distinct quantifiable spatial and geometric parameters (Fig. 4A; Table 1).

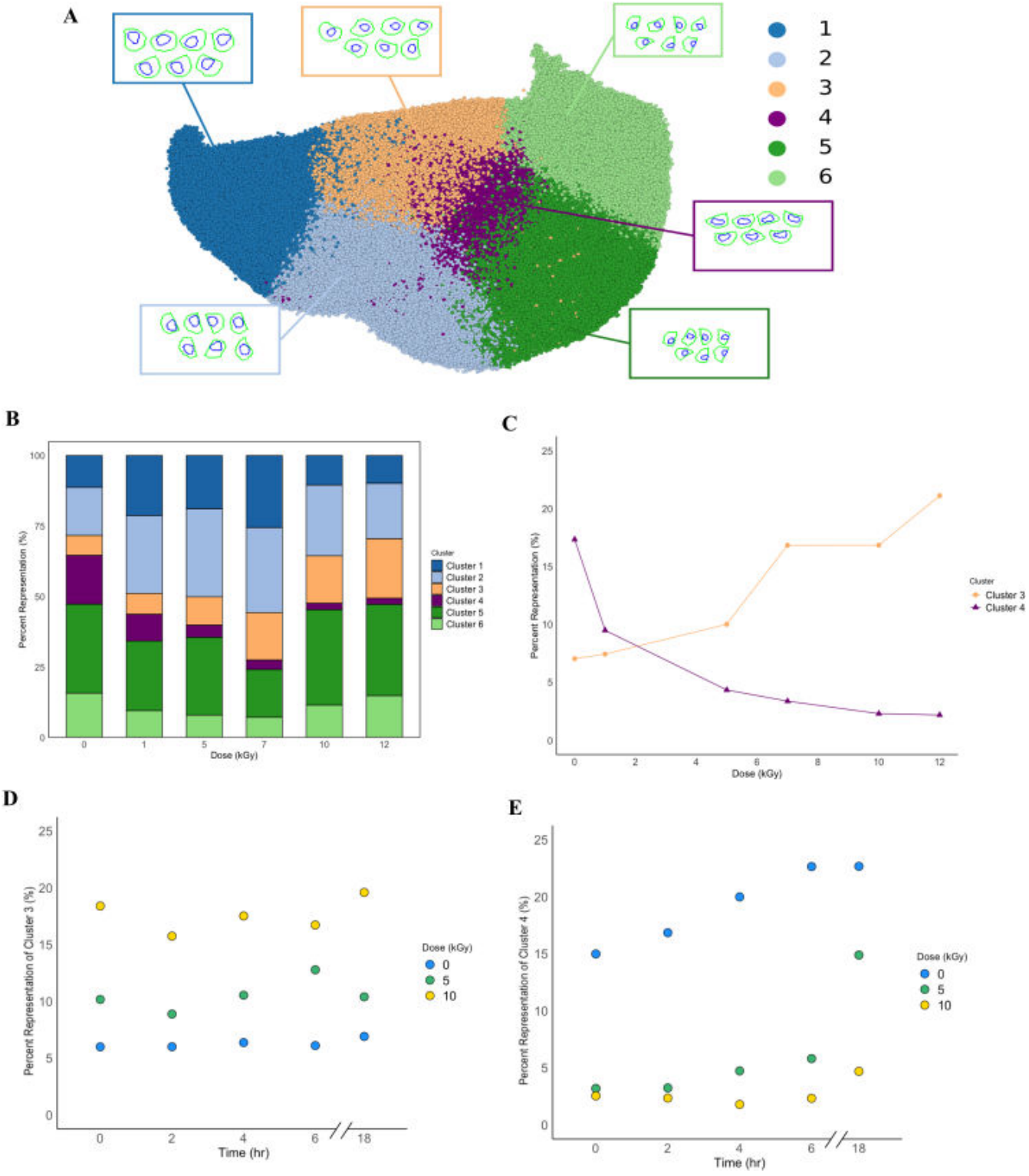

FIG 4 Morphological clustering and analysis of group representation among *D. radiodurans* cell populations. (A) 2D-UMAP construction utilizing the full data set of collected cell images. Cells are binned into one of six distinct morphological groups. (B) Morphological group representation for *D. radiodurans* wild-type strain across acute IR dose treatments. Group representation is displayed as a percentage of the total population of cells contained within each cluster defined in panel A. (C) Change in the percent representation of morphological groups 3 and 4, respectively, across acute IR dose treatment. (D) Change in the percent representation of morphological group 3 over an 18-hour recovery period for 0, 5, and 10 kGy acute IR dose treatments. (E) Change in the percent representation of morphological group 4 over an 18-hour recovery period for 0, 5, and 10 kGy acute IR dose treatments. (C) Lines are drawn as guides to the eye. (B–E) Raw percentage values are displayed in k-means enrichment tables (Fig. S13).

TABLE 1 Mean measured geometric properties of morphological groups as defined in Fig. 4A[a]

		Geometric property (average value)									
		Cell area (μm^2)		Nucleoid area (μm^2)		Nucleoid fractional area		Nucleoid circularity		Nucleoid eccentricity	
Morphological cluster	Representative morphology	Mean	SEM	Mean	SEM	Mean	SEM	Mean	SEM	Mean	SEM
1		5.4077	0.0055	1.5580	0.1184	0.6177	0.0006	0.8647	0.0006	0.2957	0.0003
2		3.6112	0.0021	1.1172	0.0392	0.5755	0.0005	0.8895	0.0005	0.3175	0.0002
3		4.1231	0.0039	0.7510	0.0509	0.5750	0.0007	0.9184	0.0006	0.1900	0.0002
4		3.0452	0.0025	0.8682	0.0573	0.8180	0.0004	0.7514	0.0007	0.2908	0.0003
5		2.4726	0.0010	0.7398	0.0218	0.5864	0.0004	0.8932	0.0004	0.3057	0.0002
6		2.0247	0.0021	0.4126	0.0269	0.6519	0.0006	0.8819	0.0007	0.2191	0.0003

[a]Standard error of the mean (SEM) shown for corresponding geometric property.

Clusters 1 and 2 were characterized by enlarged cell areas, enlarged nucleoids, and a large nucleoid fractional area. Cluster 3 had an enlarged cell area similar to that of Clusters 1 and 2 but maintained a smaller nucleoid area. It is worth noting that Cluster 3 was the most-circular morphological cluster and had the lowest nucleoid fractional area among all clusters. Cluster 4 had enlarged nucleoids and was the most eccentric geometrically; this morphology has previously been shown to be associated with active cell division and therefore perhaps active genome repair (34, 42). Finally, Clusters 5 and 6 were characterized by smaller nucleoid areas and nucleoid fractional areas than the other morphological clusters. Clusters 5 and 6 also had highly circular nucleoids. For non-irradiated *D. radiodurans* cells, Cluster 5 was the most represented morphological cluster (Fig. 4B), while Cluster 3 had the lowest representation. These cutoffs were determined entirely computationally via the k-means algorithm, which attempts to find similar groups within a population in an unsupervised manner (43, 44).

We suspected that the relative abundance, or enrichment, of these morphological clusters should be different for cell populations during recovery from exposure to ionizing radiation relative to populations of unirradiated cells. To identify dose-dependent shifts in the enrichment of morphological clusters, we first analyzed the morphological clustering of cell populations collected in the dose-dependent study of wild-type R1 (Fig. 4B). We found that Cluster 3 and Cluster 4 experienced the largest shifts across different doses (Fig. S13A). During recovery after exposure to a low dose of ionizing radiation (1 kGy), the representation of morphological Cluster 4 in wild-type *D. radiodurans* cell populations decreased nearly twofold. During recovery from irradiation after exposure to higher ionizing radiation doses (10–12 kGy), the representation of Cluster 4 decreased nearly eightfold (Fig. 4C). In contrast, representation of morphological Cluster 3 increased over twofold during recovery from 10 to 12 kGy of ionizing radiation (Fig. 4C). Representative data for Fig. 4C captures recovery after 2 hours. It is worth noting that, upon analysis of the shifts in morphological clusters (Cluster 3 and Cluster 4) across 18 hours of recovery after exposure to ionizing radiation (Fig. S13B and S14), we observed no further changes in the relative abundance of morphological Cluster 3 (Fig. 4D); this was a similar pattern to that observed for the representation of Cluster 4 over time

of recovery for the first six hours post-irradiation (Fig. 4E). However, we observed that the relative abundance of morphological Cluster 4 increased following sham irradiation (0 kGy) in the first 6 hours of recovery, after which Cluster 4 representation appeared to reach a steady state. We also observed an increase in the relative abundance of morphological Cluster 4 from 6 hours post-irradiation to 18 hours.

Screening genomic mutants of *D. radiodurans* indicates that additional nucleic-acid binding proteins and stress-response proteins affect cell population morphologies during recovery from ionizing radiation

To assess the potential role of different classes of proteins on geometric changes during recovery from ionizing radiation, we used 13 selected knockdown, UTR-deletion, or knockout of genes from four distinct classes (Table S6). Representatives of the first class, stress-response network genes included two characterized regulatory stress response proteins (PprA and IrrE/Pprl) and one characterized stress response regulatory small RNA (Dsr2/PprS) (25). Representatives of the second class, nucleic-acid-binding proteins included four proteins that (in other organisms) associate with small RNAs under stress (KhpA, KhpB, PNPase, and Rsr). The third class was composed of proteins characterized in *D. radiodurans* that have homology to known *E. coli* nucleoid-associated proteins. These proteins included three *D. radiodurans* NAPs with *E. coli* homologs (Dps1, Dps2, and RecA) and a deletion of the full 5′ regulatory untranslated region encoding for GyrA (GyrA-UTR), another predicted NAP involved in DNA repair (45). The fourth and final class was represented by known and established *D. radiodurans* NAPs (Lrp, DR_1116, and DRA_0141) (32). These 13 genomic knockouts in four categorical classes were selected from a pre-existing library or generated for this publication (Tables S6 and S7).

We first characterized the geometric properties of the mutant strains in the absence of radiation and compared these properties to those of the wild-type R1 strain. Measured changes in cell area, nucleoid area, nucleoid fractional area, nucleoid circularity, and nucleoid eccentricity are shown in Fig. S15. Mutant strains had average cell areas very similar to the wild type, with no differences greater than 20% (although some were statistically significant). In contrast, the nucleoid area and the nucleoid fractional area were at least 18% greater in at least one of the known *D. radiodurans* NAP (DRA_0141) and the tandem mutant strain of hypothesized *D. radiodurans* NAPs Dps1 and Dps2. This finding validates our ability to capture the role of these proteins in maintaining nucleoid size, even in the absence of any radiation stress. We also found a potential, not yet reported, role of KhpA and KhpB in the maintenance of nucleoid size under unstressed conditions, in the form of a 20% difference in the nucleoid area of the genomic knockout strains for these proteins. We found only minor (although statistically significant) differences of less than 10% in nucleoid eccentricity and circularity in all the mutant strains relative to the wild-type strain under these unstressed conditions.

To identify potential associations between specific proteins and response to radiation, we exposed each mutant strain to sham (no radiation) and to 10 kGy of IR. For these experiments, the wild-type strain was also simultaneously irradiated and re-characterized as an internal experimental control. We measured the relative abundance of the six morphological clusters defined above (Fig. 5A) after 2 hours of recovery from IR or sham (Fig. 5; Fig. S16). We found eight strains, *ΔDRA0141*, *ΔgyrA-UTR, Δlrp, ΔDR1116, Δpprl, ΔkhpA, ΔkhpB,* and *Δrsr,* which had at least one morphological cluster with a percent representation that was different from that of the wild type by at least a factor of two at the same dose of ionizing radiation (Fig. 5A through D; Table S8). We quantified this for each morphological cluster using a logarithmic scale, defined as log2FoldChange = log2(percent representation in mutant/percent representation in wild type). A factor of two in differences in representation corresponds to log2FoldChange (log2FC) ≥ 1 or ≤ −1. Among these eight strains, the most consistent changes, defined as a *P*-adjusted (*P*-adj) value less than 0.05, were found in six strains: *ΔDRA0141*, *ΔgyrA-UTR, Δlrp, ΔDR1116, Δpprl,* and *Δrsr* (Fig. 5A through D; Table S8).

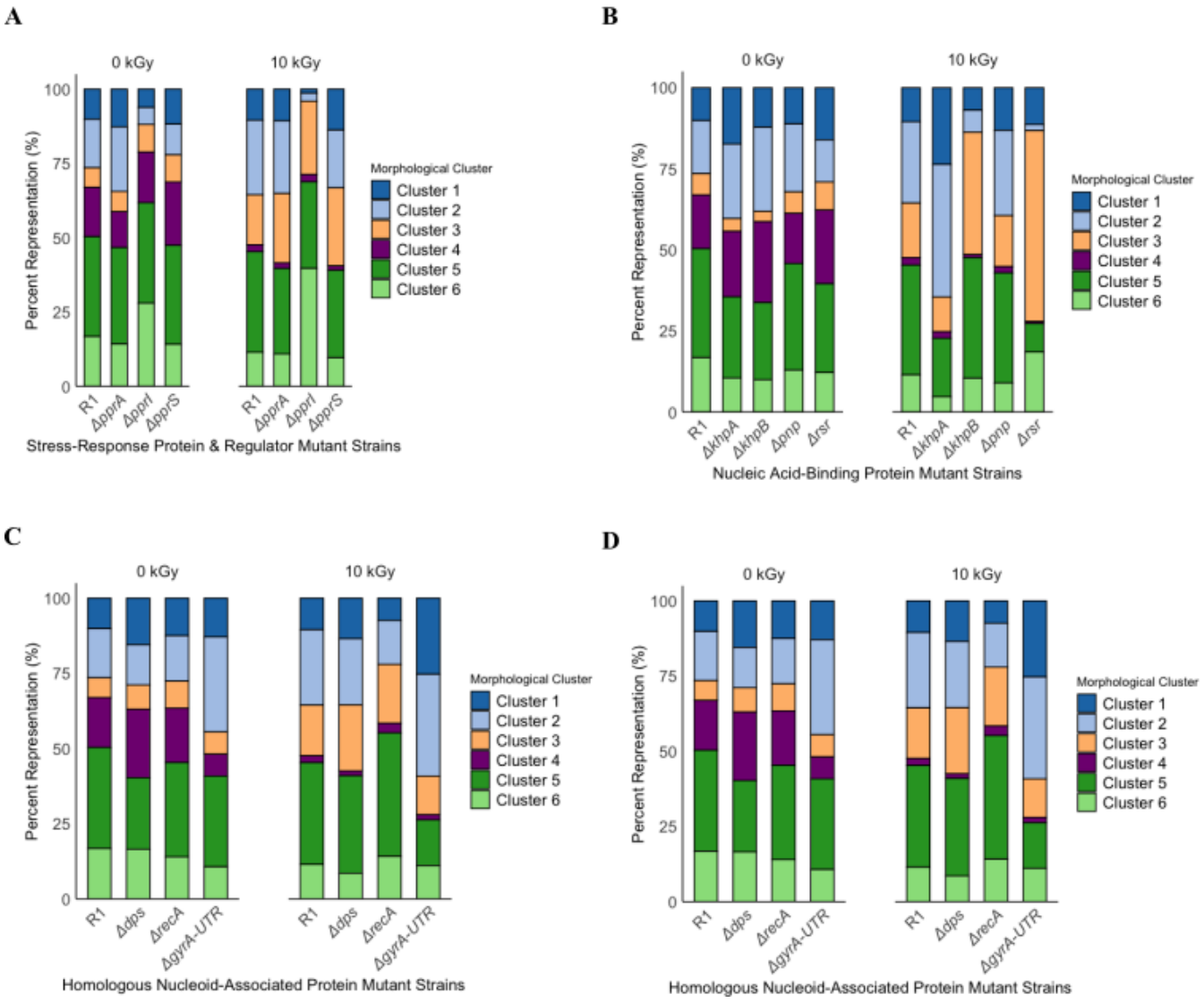

FIG 5 Shifts in morphological group representation with acute IR dose treatments for *D. radiodurans* mutant strain classes. Group representation is displayed as a percentage of the total population of cells contained within each cluster defined in Fig. 4A. (A) Stress-response proteins and regulator. (B) Nucleic acid-binding proteins. (C) *D. radiodurans* proteins with homology to *E. coli* nucleoid-associated proteins. (D) Known *D. radiodurans* nucleoid-associated proteins. (A–D) R1 data are identical across all graphs.

All mutant strains tested experienced a depletion in morphological Cluster 4 after IR exposure (Fig. 5A through D; Table S8). However, for two strains (*ΔkhpB* and *Δrsr*), we found that morphological Cluster 4 is significantly depleted (log2FoldChange ≤ −1) after IR than it is for the wild type; both KhpB and Rsr are classed as nucleic-acid-binding proteins. Additionally, we found that the mutant lacking the stress response protein Pprl had a statistically significant, log2FoldChange > 1, greater representation than the wild type in the condensed morphological extreme, Cluster 6, after irradiation (Table S8). In all three cases (mutants lacking KhpB, Rsr, or Pprl), we saw a lower representation (inverse log2Fold) of the decondensed extreme, Cluster 2 after irradiation than for the wild type after radiation (Rsr and Pprl are statistically significant—*P*.adj < 0.05) (Table S8). This suggests that deletion of the genes encoding for KhpB, Rsr, or Pprl from the *D. radiodurans* genome resulted in a greater nucleoid condensation upon exposure to IR stress.

In contrast with the three single-protein mutations that resulted in greater condensation following IR, another member of the nucleic acid-binding class (KhpA) had an opposing effect. The KhpA mutant had greater representation, log2FoldChange > 1, of Cluster 1 following IR than does the wild type; Cluster 1 is a decondensed-nucleoid morphological extreme (Table S8). Following IR, the KhpA mutant had less representation, log2FoldChange < −1, of Cluster 6 than does the wild type; Cluster 6 is a condensed-nucleoid morphological extreme (Table S8).

Among the gene deletion mutant strains evaluated in this study, we assessed the survival of the three gene deletion strains (KhpA, KhpB, and Rsr) upon exposure to sham irradiation and acute IR doses of 5 and 10 kGy (Fig. S1B). Similar to previous studies performed on other gene deletion candidates such as GyrA-UTR, PprS, and PprI, we observed a statistically significant ($P < 0.05$) decrease in overall survival upon exposure to IR when compared to the wild type (Fig. S1B) (25, 45, 46).

DISCUSSION

There are growing databases of newly discovered organisms and bacterial communities that include data sets of genomic, proteomic, and transcriptomic information (47–50). Efforts have been made to predict bacterial phenotypes from this information (51). However, dynamic phenotypic changes in nucleoid organization have not been well characterized in extremophilic organisms undergoing stress. The connection between oxidative stressors (i.e., ionizing radiation) and mechanisms of DNA protection and repair continues to be of interest, particularly in light of genome maintenance by extremophilic organisms. Unlike proteobacteria such as *E. coli*, *D. radiodurans*, a model extremophile known for its unique stress tolerance and genome maintenance mechanisms (52–55), constitutively maintains a highly condensed nucleoid. Thus far, quantitative characterization of nucleoid geometric features and their dynamics under stress has not been reported in *D. radiodurans*.

To address this gap, we have developed a high-throughput pipeline for image analysis and used it to characterize the geometric properties of the nucleoids of the extremophile bacterium *D. radiodurans*. The user-defined geometric properties that we measured are the cross-sectional area of cells and nucleoids, the ratio of nucleoid cross-sectional area to cell cross-sectional area (which we term "nucleoid fractional area"), and the circularity and eccentricity of nucleoids. We found that IR results in significant changes in the geometric properties of wild-type R1 cells. Specifically, the average cell area was greater following IR, and the average nucleoid eccentricity was lower, for all radiation doses tested (Fig. 3A; Fig. S7; Table 1). The increase in cell area is consistent with the idea that bacterial cells under stress divide less frequently and therefore may grow to larger sizes before division (37, 56). The changes in nucleoid eccentricity and circularity both point to the nucleoid becoming a more compact and spherical shape after radiative stress than before. Moreover, these changes in nucleoid geometry both showed monotonic trends with radiation dose, which may suggest a dose-dependent effect of IR on increasing compaction and sphericity in the *D. radiodurans* nucleoid (Fig. 3A). Therefore, we conclude from our work that changes in geometric measurements of morphology during an extended time after acute radiation exposures might reflect recovery from IR stress. Recovery from IR stress is of particular interest in the case of *D. radiodurans* because it has the potential to yield insight into this extremophile's unusually high tolerance of IR.

While bulk-data analysis of mean properties of the whole, consolidated population yielded general insight into the shifts in geometric properties in *D. radiodurans*, the probability-density distributions of these measurements were broad (Fig. S2 to S6). This represented a high variance in the data and suggests that the geometric properties found in these populations may be heterogeneous. To expand the insight yielded by image analysis beyond that achieved by user-defined characteristics, we used a computational modeling algorithm on a parameter space defined by 32 different morphological characteristics. This algorithm clustered the 400,000+ imaged cells into

six different morphological clusters within the 32-dimensional parameter space. One of these clusters, Cluster 4, is characterized by elongated nucleoid shapes (Fig. 4A; Table 1). Previous work has shown that elongated nucleoids are associated with cell division (34, 42) and are notably less present in bacterial populations following acute radiation (28). Thus, the depletion of morphological Cluster 4 following IR stress agrees with what is known about bacterial biology in general and also yields new insight into the response of *D. radiodurans* specifically to IR stress. Interestingly, during recovery from sham irradiation, the elongated morphological group, Cluster 4, increased in representation (Fig. S14). This could be attributed to an increase in dividing cells in the un-irradiated control group. *D. radiodurans* cells in the control group may undergo a brief recovery from any physical stress induced during transport from the irradiation facility (Materials and Methods). In contrast to Cluster 4, Cluster 3 representation was enriched by IR in a dose-dependent manner. Morphologically, Cluster 3 has the most circular nucleoid and the smallest nucleoid fractional area among the defined clusters (Table 1). Thus, Cluster 3 has the most compact nucleoid shape. The dose-dependence of Cluster 3 enrichment suggests that these geometric properties may indicate that DNA repair is aided by coalesced genomic material and the proximity of the components of polyploid, *D. radiodurans* genome, increasing the efficiency of *D. radiodurans* robust homologous recombination repair systems (57). These clear trends, with increasing IR dose, of increasing enrichment of Cluster 3 and increasing depletion of Cluster 4 appear to be signatures of recovery following radiation exposure (Fig. 4B).

Following survival comes recovery, which is a time-dependent process. *D. radiodurans*' recovery from IR-caused stress is a three-step process of DNA degradation, DNA recombination, and a resumption of DNA synthesis (52, 58). DNA degradation and delay in DNA synthesis have been shown to be dependent on radiation dose (59). Indeed, our morphological analysis showed that the timescale for recovery appeared dependent on the radiation dose (Fig. S1A). We have quantified the geometric properties of *D. radiodurans* populations over the 18 hours following IR at an intermediate dose (5 kGy) and a high dose of 10 kGy (approaching the D_{10} value of 12.5 kGy).

Our morphological analysis identified sub-population behavior not only in a dose-dependent manner but also along the *D. radiodurans* recovery timescale. Following IR exposure at 5 or 10 kGy, Cluster 3 representation was roughly constant over the next 18 hours of recovery (Fig. 4C). Thus, even hours after radiation exposure, *D. radiodurans* cells had compacted nucleoids, as indicated by the low nucleoid fractional area and highly circular nucleoid characterizing morphological Cluster 3. We speculate that this morphological cluster could act as an identifiable long-term marker of DNA damage induced by IR.

If the geometric changes observed following radiation are linked to the activity of the molecular machinery for DNA repair and recovery, it is plausible that changes in this machinery may be reflected in *D. radiodurans*' structural characteristics even in the absence of radiation stress. Prior studies have identified several gene products that may impact nucleoid organization and structure (32, 45). We evaluated 13 selective genomic mutant strains with deletions or mutations to genes that encode for proteins involved in stress response, binding to DNA or RNA, and nucleoid association (Table S6). For every mutant strain tested, at least one user-defined geometric property was significantly different from the corresponding property in the wild type (Fig. S16). These data suggested that the morphological clusters will differ in the absence of these gene products when compared to wild type.

Computational morphological clustering has the potential to yield insight into the roles of specific gene products both in *D. radiodurans*' resilience to radiative stress and in regard to this organism's constitutively condensed nucleoid. Knocking out such gene products resulted in several cases where the population of these morphologically extreme clusters was shifted from that of the wild-type R1. These shifts could be seen in the changes in representation by morphologically extreme clusters upon gene deletion at sham conditions (Fig. S16). These morphologically extreme clusters are Clusters 1,

2, and 6. Clusters 1 and 2 are characterized by a large nucleoid and large nucleoid fractional area; Cluster 6 has a small nucleoid and small nucleoid fractional area (Table 1). Notably, these shifts were often in accord across clusters—in such cases, Clusters 1 and 2 increased or decreased together, and Cluster 6 decreased or increased inversely (Fig. 5). However, in other cases, Cluster 2 increased, while Cluster 1 was largely unchanged. The contrast between correlated and anti-correlated shifts for Clusters 1 and 2 showed the potential of this approach to yield insight into different molecular mechanisms underlying the maintenance of *D. radiodurans'* constitutively condensed nucleoid.

Surprisingly, deletions in genes encoding proteins previously described as nucleoid-associated in *E. coli* or *D. radiodurans* were much less impactful on morphology than were deletions in stress-response and nucleic acid-binding proteins. Of the nucleoid-associated proteins studied, only one, DR_1116, differed from the wild type by log2Fold in morphological representation following IR exposure. Rather, the deletion of genes encoding nucleic acid-binding and stress response classes of proteins observed in this study, specifically KhpA, KhpB, Rsr, and PprI, appeared to have the most notable effects on *D. radiodurans* nucleoid morphology following IR. Additionally, we observed significant decreases in the survival fraction of these strains post-IR exposure (Fig. S1B). The mutant deficient in the gene encoding KhpA, with the greatest representation in the less-condensed nucleoid morphological clusters, appeared to be the most radiosensitive when compared to the strains enriched in condensed nucleoid morphological clusters (KhpB and Rsr) and the wild type. Importantly, these proteins were not previously known to play a role in controlling nucleoid dynamics and condensation in bacterial populations. Although proteins like KhpB could contribute additional (yet to be described) roles in radiation resistance in *D. radiodurans,* these data suggest that they may play critical, undescribed roles in dynamic nucleoid regulation, and thus IR stress resistance, meriting further study. The fact that the absence of these proteins could affect nucleoid condensation by both direct and indirect mechanisms (i.e., regulation of other cell factors) also merits additional investigation.

Interestingly, *ΔgyrA-UTR,* exhibited a phenotype under IR stress of various cell membrane protrusions (Fig. S17). This phenotype appears similar to blebbing behavior, typically seen in mammalian cells under apoptosis, stem-cell differentiation, and other "cell-fate" determination states (60). While quantitative determination of blebbing for the purpose of tracking signaling pathway activation has occurred in mammalian cells (61–63), this method of spatiotemporal organization analysis has not yet been utilized in bacteria. These results warrant further exploration as they may provide insight into potential signaling pathways in *Deinococcus* under IR stress.

Within the context of our investigation into responses to radiation, the presence of dead cells introduces a potential complication in accurately assessing population-level shifts in morphological phenotypes in response to varying doses of radiation. Despite the inherent challenge posed by the presence of dead cells, our robust analysis of a significant number of cells within each dose group still affords us the capacity to discern and characterize these morphological alterations. Future iterations of this work could involve refining our methodology to distinguish between live and dead cells, particularly within the specific framework of radiation dose-response studies. Such enhancements would not only bolster the precision of our findings but also provide valuable insights into the nuanced interplay between radiation exposure, cell death, and the resulting morphological changes within *D. radiodurans* cell population.

We expect that the method we present here should be able to be used in the analysis of other prokaryotes to measure the geometric properties of cells and nucleoids. For the nucleoid in particular, geometric parameters such as compactness and size impact biological processes essential to genome repair through mechanisms such as restricted diffusion and crowding (64, 65). The approach we present here can be used to measure changes in nucleoid compaction, as well as other morphological changes, across different organisms to provide new insight into their stress response mechanisms and their survival. It also has the potential to be combined with more standard genetics

techniques to yield insight into the regulation of subcellular compartmentalization in a wide range of bacteria.

Furthermore, the analysis techniques used here are not specific to bacteria; this approach should be directly extensible to a wide range of organism types and to types of subcellular structures that are not nucleoids or contain DNA. Given the differences across organisms in chromosomal size, genome copy numbers, and survivability, the connection between the dynamics of nucleoid organization and the presence of extreme phenotypic traits in bacteria remains intriguing. Geometric parameters such as compactness and size impact biological processes essential to genome repair such as restricted diffusion and crowding (64, 65), thus quantifying nucleoid compaction activity across different organisms is a key aspect of understanding their stress response mechanisms and their survival. Therefore, the work presented here can be used to probe morphological features at the subcellular level and expose biophysical phenomena not readily recognizable otherwise.

The utility of this method is likely to be increased by the use of high-resolution and super-resolution imaging techniques, which will make finer gradations in geometry distinguishable and may allow the possibility of examining an even higher-dimensional morphological space.

Conclusion

We created a robust image analysis methodology to elucidate quantitative features of bacterial cell and nucleoid morphology. These methods allowed quantitative analysis of geometric changes in the cell envelope structure and the nucleoid structure of the extremophile bacteria *D. radiodurans* following ionizing radiation and genomic deletion of key candidate proteins. We find dose- and time-dependent changes in the cell and nucleoid morphologies. The methods create a useful screening tool to probe subcellular organization and its regulation, response to stress, and possible mechanistic roles of genome-associated proteins in nucleoid condensation.

MATERIALS AND METHODS

Bacterial cultures and growth conditions

Escherichia coli strain DH10b and its plasmid-containing derivatives were grown at 37°C in Luria-Bertani (LB) media broth (10 g/L tryptone, 10 g/L NaCl, and 5 g/L yeast extract) or LB solid (1.5% agar) medium. When necessary, chloramphenicol was used at a concentration of 34 µg/mL for *E. coli* strains. *Deinococcus radiodurans* strain R1 (ATCC 13939) and its plasmid-containing derivatives were grown at 32°C in TGY broth (1% tryptone, 0.1% glucose, and 0.5% yeast extract) or TGY solid (1.5% agar) medium. When necessary, antibiotics were used at a concentration of 16 µg/mL (kanamycin and tetracycline) and 3.4 µg/mL (chloramphenicol) for *D. radiodurans* strains. All strains are listed in Table S6.

Transformation of recombinant plasmids in *D. radiodurans*

Recombinant plasmids were transformed into *D. radiodurans* as previously described (45). *D. radiodurans* cells were grown to the late log phase (OD_{600} = 1.0) and mixed with 30 mM $CaCl_2$ and 10% glycerol. For transformation into the competent cell stock, 1.5 µg plasmid DNA was added, followed by an incubation of 1 hour on ice, and a subsequent incubation at 32°C for 1 hour. Cells were then incubated at 32°C shaking overnight in 800 µL of fresh TGY media in test tubes. Post-incubation, cells were plated onto TGY plates with the appropriate antibiotic concentration (above) and incubated for 3 days at 32°C. Transformants were verified via polymerase chain reaction (PCR) and sequencing (SNPsaurus).

Construction of genomic knockout strains in *D. radiodurans*

The knockout strains of *D. radiodurans* were constructed using a homologous recombination method reported previously (26). In short, 1 kb regions upstream and downstream from the gene selected for deletion were amplified via PCR from the R1 genome and cloned into the pUC19mPhes plasmid alongside a fragment containing a kanamycin cassette, as well as lox66 and lox71 sequences. All fragments were then gel-purified using QIAquick Gel Extraction Kit (Qiagen) and assembled with HindIII-digested pUC19mPheS plasmid using NEBuilder HiFi DNA Assembly Master Mix (New England Biolabs Inc.). The resulting plasmid was then transformed into *E. coli* DH10b strain for isolation via QIAprep Plasmid Mini-Prep Kit (Qiagen). The isolated plasmid was subsequently transformed into *D. radiodurans* R1 chemically competent cells (above). Mutant strains were selected on TGY plates with the appropriate kanamycin concentration and 4-chlorophenylalanine (5 mM) for three to five rounds of selection. The total process selected for cells that underwent homologous recombination to replace the target region with the kanamycin cassette and no longer contained the pUC19mPheS recombinant plasmid. The kanamycin resistance marker was removed using Cre/Lox recombination, after the transformation of the pDeinoCre plasmid into competent cells of the deletion strain (above). The primers used for these processes are included in Table S7. All plasmids are listed in Table S6.

Exposure of bacteria to ionizing radiation

For acute IR exposures, 5 mL of exponential phase cells (OD_{600} = 0.8, 6.4×10^8 cells/sample) was irradiated with a 10 MeV, 18-kW linear accelerator (LINAC) β-ray source at target doses ranging from 0 to 12 kGy (250 Gy/s) at the National Center for Electron Beam Research, Texas A&M University, as reported previously (25, 45, 66). It is worth noting that as shown in the recorded dosimetry data (Table S10), as expected, small variations were present within the actual delivered doses at the radiation facility. Samples were kept in stasis on dry ice during transport to and from the irradiation facility (~2 hour each way). Irradiated samples were then incubated in TGY broth for no additional recovery time (for survival assays and growth assays) or 2 hour (for staining and imaging) at 32°C immediately following irradiation and transport. Exact acute IR dose exposures and dose ranges for each day of experimentation are located in Table S10.

Survival assays during recovery post-IR

To measure survival following acute IR exposures, biological replicas in triplicate of exponential phase cells (OD_{600} = 0.8) were irradiated with a 10 MeV, 18-kW LINAC β-ray source at doses 0, 1, 5, 7, 10, and 12 kGy (250 Gy/s) at the National Center for Electron Beam Research, Texas A&M University as reported previously (25, 45, 66). Following irradiation at room temperature and transport, samples were immediately serially diluted (10^{-0} to 10^{-3}), and 10 µL of the dilution was plated onto TGY agar plates. Plates were incubated at 32°C for 2 days, and colonies were counted for the 10^{-3} dilution. Relative survival rates were defined as the percentage of colony-forming units observed under each IR dose condition compared to samples that received no IR.

Growth assays during recovery post-IR

Growth curves of R1 at variable kGy dosages were evaluated using a Plate Reader (BioTek), and OD_{600} was calculated using a bacterial calibration curve for *D. radiodurans* strains. Following irradiation at room temperature and transport, samples were immediately incubated in culture tubes at 32°C. Biological replicates of each strain (25 µL), at each dose, in technical triplicate, were distributed into 96-well plates (Greiner Bio-One µClear Bottom 96-well Polystyrene Microplates) with 175 µL of TGY media. OD_{600} of each sample was measured every 2 hours for 18 hours as the cultures grew with shaking at 32°C, and the average of all replicas per strain, per dose condition, was calculated.

Staining protocol

Cells were stained using a 3 mM stock solution of Nile Red (Thermo Fisher, Invitrogen) (used for staining membranes) and 15 µM stock of Syto 9 green nucleic acid stain (Thermo Fisher, Invitrogen) (used for staining nucleoids). Stock solutions of Nile Red were made by dissolving solid Nile Red stain into DMSO at a concentration of 3 mM. Stock solutions of Syto 9 were diluted to 15 µM from factory stock into DMSO. In 1 mL of cell culture, final concentrations of Nile Red and Syto 9 were 30 µM and 150 nM, respectively. Cells were then placed in a rotary shaker for 30 min at 32°C. Cells were then pelleted, and the stain solution was removed. The cell pellet was then resuspended in 200 µL of Dulbecco's phosphate buffer solution. Cell suspensions were then prepared for imaging by placing 15 µL of cell solution onto a microscope slide with an image spacer (Grace Bio-Labs) and a #1 size coverslip (Fisher Scientific).

Imaging

Microscopy was done via confocal microscopy using a FluoView 1000 confocal microscope on an Olympus IX81 microscope base. The 488 and 543 nm laser lines were used. The FluoView settings are described in Table 2.

Image analysis protocol

Z-stack images are opened in FIJI, which is an open-source, free image analysis software (67). The z-slice that is at the midpoint of the cells is found by iterating through the z stack and picking the midpoint by eye. This slice is then saved into two parts, a membrane image and a nucleoid image. These images are saved with the same name as the z-stack with the suffixes "_mem.tif" and "_nuc.tif," respectively. The rest of the analysis is done in a Python (https://ipython.org) Jupyter notebook (68, 69). The notebook opens the images and creates a composite image with one channel being the membrane image and the other being the nucleoid image. These composite images are then segmented using the Cellpose application programming interface (36). The nucleoids are segmented using the "nuclei" model in Cellpose with the initial diameter set to 9 pixels and flow_threshold equal to 0.4. The cells are segmented using the "cyto" model using both the membrane channel and the nucleoid channel, with an initial diameter set to 13 pixels and flow_threshold equal to 0.4. The masks from each model evaluation are saved with the suffixes "_nuclei_mask.tif" and "_cell_mask.tif" respectively. These masks then go through a process of connecting the nuclei and cell masks. The connecting process does the following: ensure each nucleoid and cell are matched 1:1 with the same pixel value, ensure no two nuclei are within a cell, and ensure nuclei are not bigger than the cell. These masks are then used to get the region properties of each cell/nucleoid pair. The physical quantities measured are nucleoid circularity, nucleoid eccentricity, nucleoid area, cell area, and nucleoid fractional area. Total cells imaged in these analyses for all experiments are located in Table S11.

Calculation of geometric properties

The area and perimeter of each nucleoid mask can be used to find its circularity as follows: $\text{circularity} = \frac{4\pi \cdot \text{area}}{\text{perimeter}^2}$. Circularity measures the degree to which the geometry of the nucleoid mask approaches a mathematically perfect circle, for

TABLE 2 Confocal microscope software settings[a]

Laser (nm)	Power (%)	PMT voltage (V)	Gain	Offset (%)
488	5	350–450	1×	20
543	15	600–700	1.5×	20

[a]PMT voltage is provided as a range due to voltage variation required for a low saturation of pixels. Voltage selection is performed via adjustment of the HiLo LUT edit setting and changing the voltage to provide a minimal number of red pixels while maximizing grayscale pixels.

$\text{area} = \pi r^2$ and $\text{perimeter} = 2\pi r$, where r is the radius of the circle. Circularity has a value of one for a perfect circle, which is the shape that maximizes the area-to-perimeter ratio. Thus, as the nucleoid becomes more compact, the circularity will increase. Artifacts in our analyses of digital images of nucleoids can give circularity values greater than one as follows: The digital nucleoid mask is made of square pixels. The perimeters of the nucleoid masks are estimated using a built-in function in the scikit image library in Python. Parts of the mask pixels can lie outside the bounds of the estimated perimeter. If enough mask area is located outside the estimated parameter, a circularity value greater than one will be calculated. This artifact will consistently act to shift calculated circularity values higher than the true value. However, the consistent direction of this shift means that circularity as used here is still a valid measure of the relative compactness of nucleoids.

Eccentricity is measured by fitting an ellipse to the outside edge of the nucleoid mask. A non-circular ellipse has two perpendicular axes with different lengths, $a > b$. Eccentricity e arises from the difference in these two lengths, thus: $e = \sqrt{1 - \frac{b^2}{a^2}}$. For a circle, $a = b$. As the nucleoid becomes less elongated, eccentricity will decrease toward zero (Fig. 2B, right side).

Statistics

Statistical analysis was done in Python using the scipy stats library. The Kolmogorov-Smirnov test was done using the kstest function. Student's *t*-test was calculated with the ttest_1samp function. ANOVA test was calculated with f_oneway function. The number of cells per biological replicate can be found in Table S11. For each of the morphological clusters, pair-wise comparisons of relative abundance, using a *t*-test, were made between the R1 data and the mutant strains. For example, the relative abundance of Cluster 1 across the R1 samples was compared against the relative abundance of Cluster 1 across the *ΔkhpA* samples. A Bonferroni correction was applied to the resulting *P*-values to correct for the large number of comparisons. Clusters from mutant strains with a change in a relative abundance ±Log2 of 1 and with an adjusted *P*-value below 0.05 are reported as significantly different than R1 (Table S9).

Morphological analysis

A total of 32 key morphological parameters encompassing both nuclear and cellular features were extracted from individual cells using a Cell Profiler pipeline (41) (Table S5). The optimal number of clusters was determined using the "elbow method," or the beginning of the elbow of the inertia/silhouette graph shown in Fig. S18. Cluster partitioning was determined by the k-means algorithm, an unsupervised approach that only requires the number of clusters to be input by the user (43, 44). Approximately 470,000 cells encompassing all experimental conditions were used to capture the entirety of possible morphological phenotypes. To standardize the data set, morphological parameters were log-normalized and standard scaled (to account for parameters of different orders of magnitude). The data set was then used to construct a 2D-Uniform Manifold and Projection space (70). UMAP is a nonlinear dimensionality reduction algorithm that seeks to capture the structure of high dimensional data in a lower-dimensionality space (for this work, the 32-vector space was simplified to two). Each point in the space represents an individual cell whose morphological properties have been projected. As a synergistic approach to UMAP, k-means clustering, an unsupervised hierarchical clustering algorithm, was performed on the normalized data set to discretize unique morphological clusters. The algorithm converged on six optimal clusters based on a plateau of inertia and silhouette values (Fig. S18), and these clusters were projected onto the UMAP space for visualization. Together, each individual cell expressed a unique position on the UMAP space and belonged to a k-means morphological cluster. Condition-specific morphological quantification was determined by the ensemble effects of individual cells within that condition. Given the quantity of cells

for this analysis, kernel density estimation with Gaussian priors was used to construct contour maps to identify "hot zones" in the UMAP for certain conditions.

ACKNOWLEDGMENTS

We thank the Contreras Group for assistance with overnight *D. radiodurans* growth curves and radiation experiments, especially Trevor Simmons. We would like to thank Gina Partipilo for assistance in developing standardized curves for our plate reader assays. We also thank Bryan Dinh for fluorescence microscopy assistance. We additionally thank Jazmine Johnson and Jennah Johnson for their assistance in culturing *Deinococcus radiodurans* strains for this work. We also thank Dr. Pascale Servant (Université Paris-Saclay), Dr. Michael Daly (Uniformed Services University), and Dr. Suzanne Sommer (Institut de Génétique et Microbiologie - Université Paris-Sud) for their generosity in previously providing us with the following *Deinococcus* mutants used in this study—Δ*dps* (GY13314), Δ*pprI* (GY14127), and Δ*recA* (recA30).

Figure 1A and 2B were created with BioRender.com.

This work was supported by the Air Force Office of Scientific Research (Grant FA9550-20-1-0131) and the Welch Foundation (Grant F-1756). A.C. was supported by the National Science Foundation Graduate Research Fellowships (Grant DGE-2137420).

AUTHOR AFFILIATIONS

[1]Interdisciplinary Life Sciences Graduate Program, Department of Molecular Biosciences, The University of Texas at Austin, Austin, Texas, USA
[2]Interdisciplinary Life Sciences Graduate Program, The University of Texas at Austin, Austin, Texas, USA
[3]Department of Physics, Center for Nonlinear Dynamics, The University of Texas at Austin, Austin, Texas, USA
[4]Department of Chemical and Biomolecular Engineering, Whiting School of Engineering, Johns Hopkins University, Baltimore, Maryland, USA
[5]Department of Biomedical Engineering, Institute for Nanobiotechnology, Whiting School of Engineering, Johns Hopkins University, Baltimore, Maryland, USA
[6]LaMontagne Center for Infectious Disease, The University of Texas at Austin, Austin, Texas, USA
[7]McKetta Department of Chemical Engineering, The University of Texas at Austin, Austin, Texas, USA

AUTHOR ORCIDs

Antonio Cordova http://orcid.org/0009-0006-0147-5536
Philip Sweet http://orcid.org/0000-0002-0802-693X
Vernita Gordon http://orcid.org/0000-0002-5989-9378
Lydia M. Contreras http://orcid.org/0000-0001-5010-5511

FUNDING

Funder	Grant(s)	Author(s)
DOD | USAF | AMC | Air Force Office of Scientific Research (AFOSR)	FA9550-20-1-0131	Vernita Gordon Lydia M. Contreras Antonio Cordova Brandon Niese
Welch Foundation (The Welch Foundation)	F-1756	Lydia M. Contreras
NSF | National Science Foundation Graduate Research Fellowship Program (GRFP)	DGE- 2137420	Antonio Cordova

DATA AVAILABILITY

The authors confirm that the data supporting the findings of this study are available within the article and its supplemental material. The code used to generate data sets from microscopy images can be found at github.com/bniese/drad-image-analysis.

ADDITIONAL FILES

The following material is available online.

Supplemental Material

Supplemental figures (AEM00108-24-s0001.docx). Figures S1 to S18.
Supplemental tables (AEM00108-24-s0002.xlsx). Tables S1 to S11.

REFERENCES

1. Dame RT, Rashid F-ZM, Grainger DC. 2020. Chromosome organization in bacteria: mechanistic insights into genome structure and function. Nat Rev Genet 21:227–242. https://doi.org/10.1038/s41576-019-0185-4
2. Verma SC, Qian Z, Adhya SL. 2019. Architecture of the *Escherichia coli* nucleoid. PLoS Genet 15:e1008456. https://doi.org/10.1371/journal.pgen.1008456
3. Badrinarayanan A, Le TBK, Laub MT. 2015. Bacterial chromosome organization and segregation. Annu Rev Cell Dev Biol 31:171–199. https://doi.org/10.1146/annurev-cellbio-100814-125211
4. Qian Z, Macvanin M, Dimitriadis EK, He X, Zhurkin V, Adhya S. 2015. A new noncoding RNA arranges bacterial chromosome organization. mBio 6:e00998-15. https://doi.org/10.1128/mBio.00998-15
5. Hołówka J, Zakrzewska-Czerwińska J. 2020. Nucleoid associated proteins: the small organizers that help to cope with stress. Front Microbiol 11:590. https://doi.org/10.3389/fmicb.2020.00590
6. Song D, Loparo JJ. 2015. Building bridges within the bacterial chromosome. Trends Genet 31:164–173. https://doi.org/10.1016/j.tig.2015.01.003
7. Wang G, Maier RJ. 2015. Bacterial histone-like proteins: roles in stress resistance. Curr Genet 61:489–492. https://doi.org/10.1007/s00294-015-0478-x
8. Qian Z, Zhurkin VB, Adhya S. 2017. DNA-RNA interactions are critical for chromosome condensation in *Escherichia coli*. Proc Natl Acad Sci U S A 114:12225–12230. https://doi.org/10.1073/pnas.1711285114
9. Nguyen HH, de la Tour CB, Toueille M, Vannier F, Sommer S, Servant P. 2009. The essential histone-like protein HU plays a major role in *Deinococcus radiodurans* nucleoid compaction. Mol Microbiol 73:240–252. https://doi.org/10.1111/j.1365-2958.2009.06766.x
10. Frenkiel-Krispin D, Levin-Zaidman S, Shimoni E, Wolf SG, Wachtel EJ, Arad T, Finkel SE, Kolter R, Minsky A. 2001. Regulated phase transitions of bacterial chromatin: a non-enzymatic pathway for generic DNA protection. EMBO J 20:1184–1191. https://doi.org/10.1093/emboj/20.5.1184
11. Martinez A, Kolter R. 1997. Protection of DNA during oxidative stress by the nonspecific DNA-binding protein Dps. J Bacteriol 179:5188–5194. https://doi.org/10.1128/jb.179.16.5188-5194.1997
12. Levin-Zaidman S, Frenkiel-Krispin D, Shimoni E, Sabanay I, Wolf SG, Minsky A. 2000. Ordered intracellular RecA-DNA assemblies: a potential site of *in vivo* RecA-mediated activities. Proc Natl Acad Sci U S A 97:6791–6796. https://doi.org/10.1073/pnas.090532397
13. Morikawa K, Ohniwa RL, Kim J, Maruyama A, Ohta T, Takeyasu K. 2006. Bacterial nucleoid dynamics: oxidative stress response in *Staphylococcus aureus*. Genes Cells 11:409–423. https://doi.org/10.1111/j.1365-2443.2006.00949.x
14. Smith BT, Grossman AD, Walker GC. 2002. Localization of UvrA and effect of DNA damage on the chromosome of *Bacillus subtilis*. J Bacteriol 184:488–493. https://doi.org/10.1128/JB.184.2.488-493.2002
15. Trojanowski D, Kołodziej M, Hołówka J, Müller R, Zakrzewska-Czerwińska J. 2019. Watching DNA replication inhibitors in action: exploiting time-lapse microfluidic microscopy as a tool for target-drug interaction studies in *Mycobacterium*. Antimicrob Agents Chemother 63:10. https://doi.org/10.1128/AAC.00739-19
16. Hada M, Georgakilas AG. 2008. Formation of clustered DNA damage after high-LET irradiation: a review. J Radiat Res 49:203–210. https://doi.org/10.1269/jrr.07123
17. Daly MJ. 2009. A new perspective on radiation resistance based on *Deinococcus radiodurans*. Nat Rev Microbiol 7:237–245. https://doi.org/10.1038/nrmicro2073
18. Ghosal D, Omelchenko MV, Gaidamakova EK, Matrosova VY, Vasilenko A, Venkateswaran A, Zhai M, Kostandarithes HM, Brim H, Makarova KS, Wackett LP, Fredrickson JK, Daly MJ. 2005. How radiation kills cells: survival of *Deinococcus radiodurans* and *Shewanella oneidensis* under oxidative stress. FEMS Microbiol Rev 29:361–375. https://doi.org/10.1016/j.femsre.2004.12.007
19. van Gerwen SJ, Rombouts FM, van't Riet K, Zwietering MH. 1999. A data analysis of the irradiation parameter D_{10} for bacteria and spores under various conditions. J Food Prot 62:1024–1032. https://doi.org/10.4315/0362-028x-62.9.1024
20. Cox MM, Battista JR. 2005. *Deinococcus radiodurans* - the consummate survivor. Nat Rev Microbiol 3:882–892. https://doi.org/10.1038/nrmicro1264
21. Basu B, Apte SK. 2012. Gamma radiation-induced proteome of *Deinococcus radiodurans* primarily targets DNA repair and oxidative stress alleviation. Mol Cell Proteomics 11:M111. https://doi.org/10.1074/mcp.M111.011734
22. Liu Y, Zhou J, Omelchenko MV, Beliaev AS, Venkateswaran A, Stair J, Wu L, Thompson DK, Xu D, Rogozin IB, Gaidamakova EK, Zhai M, Makarova KS, Koonin EV, Daly MJ. 2003. Transcriptome dynamics of *Deinococcus radiodurans* recovering from ionizing radiation. Proc Natl Acad Sci U S A 100:4191–4196. https://doi.org/10.1073/pnas.0630387100
23. Makarova KS, Aravind L, Wolf YI, Tatusov RL, Minton KW, Koonin EV, Daly MJ. 2001. Genome of the extremely radiation-resistant bacterium *Deinococcus radiodurans* viewed from the perspective of comparative genomics. Microbiol Mol Biol Rev 65:44–79. https://doi.org/10.1128/MMBR.65.1.44-79.2001
24. Passot FM, Nguyen HH, Dard-Dascot C, Thermes C, Servant P, Espéli O, Sommer S. 2015. Nucleoid organization in the radioresistant bacterium *Deinococcus radiodurans*. Mol Microbiol 97:759–774. https://doi.org/10.1111/mmi.13064
25. Villa JK, Han R, Tsai C-H, Chen A, Sweet P, Franco G, Vaezian R, Tkavc R, Daly MJ, Contreras LM. 2021. A small RNA regulates *pprM*, a modulator of pleiotropic proteins promoting DNA repair, in *Deinococcus radiodurans* under ionizing radiation. Sci Rep 11:12949. https://doi.org/10.1038/s41598-021-91335-8
26. Han R, Fang J, Jiang J, Gaidamakova EK, Tkavc R, Daly MJ, Contreras LM. 2020. Signal recognition particle RNA contributes to oxidative stress response in *Deinococcus radiodurans* by modulating catalase localization. Front Microbiol 11:613571. https://doi.org/10.3389/fmicb.2020.613571
27. Tsai C-H, Liao R, Chou B, Contreras LM. 2015. Transcriptional analysis of *Deinococcus radiodurans* reveals novel small RNAs that are differentially expressed under ionizing radiation. Appl Environ Microbiol 81:1754–1764. https://doi.org/10.1128/AEM.03709-14

28. Zimmerman JM, Battista JR. 2005. A ring-like nucleoid is not necessary for radioresistance in the *Deinococcaceae*. BMC Microbiol 5:17. https://doi.org/10.1186/1471-2180-5-17
29. Maurya GK, Chaudhary R, Pandey N, Misra HS. 2021. Molecular insights into replication initiation in a multipartite genome harboring bacterium *Deinococcus radiodurans*. J Biol Chem 296:100451. https://doi.org/10.1016/j.jbc.2021.100451
30. Hansen MT. 1978. Multiplicity of genome equivalents in the radiation-resistant bacterium *Micrococcus radiodurans*. J Bacteriol 134:71–75. https://doi.org/10.1128/jb.134.1.71-75.1978
31. Harsojo, Kitayama S, Matsuyama A. 1981. Genome multiplicity and radiation resistance in *Micrococcus radiodurans*. J Biochem 90:877–880. https://doi.org/10.1093/oxfordjournals.jbchem.a133544
32. Toueille M, Mirabella B, Guérin P, Bouthier de la Tour C, Boisnard S, Nguyen HH, Blanchard L, Servant P, de Groot A, Sommer S, Armengaud J. 2012. A comparative proteomic approach to better define *Deinococcus* nucleoid specificities. J Proteomics 75:2588–2600. https://doi.org/10.1016/j.jprot.2012.03.002
33. Eltsov M, Dubochet J. 2005. Fine structure of the *Deinococcus radiodurans* nucleoid revealed by cryoelectron microscopy of vitreous sections. J Bacteriol 187:8047–8054. https://doi.org/10.1128/JB.187.23.8047-8054.2005
34. Floc'h K, Lacroix F, Servant P, Wong Y-S, Kleman J-P, Bourgeois D, Timmins J. 2019. Cell morphology and nucleoid dynamics in dividing *Deinococcus radiodurans*. Nat Commun 10:3815. https://doi.org/10.1038/s41467-019-11725-5
35. Shashidhar R, Kumar SA, Misra HS, Bandekar JR. 2010. Evaluation of the role of enzymatic and nonenzymatic antioxidant systems in the radiation resistance of *Deinococcus*. Can J Microbiol 56:195–201. https://doi.org/10.1139/w09-118
36. Stringer C, Wang T, Michaelos M, Pachitariu M. 2021. Cellpose: a generalist algorithm for cellular segmentation. Nat Methods 18:100–106. https://doi.org/10.1038/s41592-020-01018-x
37. Sweet P, Blacutt J, Gordon V, Contreras L. 2023. Exposure of *Shewanella oneidensis* MR-1 to sublethal doses of ionizing radiation triggers short-term SOS activation and longer-term prophage activation. Appl Environ Microbiol 89:e0171622. https://doi.org/10.1128/aem.01716-22
38. Bakhtiari LA, Wells MJ, Gordon VD. 2021. High-throughput assays show the timescale for phagocytic success depends on the target toughness. Biophys Rev (Melville) 2:031402. https://doi.org/10.1063/5.0057071
39. Kovach K, Davis-Fields M, Irie Y, Jain K, Doorwar S, Vuong K, Dhamani N, Mohanty K, Touhami A, Gordon VD. 2017. Evolutionary adaptations of biofilms infecting cystic fibrosis lungs promote mechanical toughness by adjusting polysaccharide production. NPJ Biofilms Microbiomes 3:1. https://doi.org/10.1038/s41522-016-0007-9
40. Brumwell SL, Van Belois KD, Nucifora DP, Karas BJ. 2023. SLICER: a seamless gene deletion method for *Deinococcus radiodurans*. Biodes Res 5:0009. https://doi.org/10.34133/bdr.0009
41. Stirling DR, Swain-Bowden MJ, Lucas AM, Carpenter AE, Cimini BA, Goodman A. 2021. CellProfiler 4: improvements in speed, utility and usability. BMC Bioinformatics 22:433. https://doi.org/10.1186/s12859-021-04344-9
42. Chien AC, Hill NS, Levin PA. 2012. Cell size control in bacteria. Curr Biol 22:R340–R349. https://doi.org/10.1016/j.cub.2012.02.032
43. Maity D, Sivakumar N, Kamat P, Zamponi N, Min C, Du W, Jayatilaka H, Johnston A, Starich B, Agrawal A, Riley D, Venturutti L, Melnick A, Cerchietti L, Walston J, Phillip JM. 2022. Profiling dynamic patterns of single-cell motility. bioRxiv. https://doi.org/10.1101/2022.09.21.508955
44. Phillip JM, Han K-S, Chen W-C, Wirtz D, Wu P-H. 2021. A robust unsupervised machine-learning method to quantify the morphological heterogeneity of cells and nuclei. Nat Protoc 16:754–774. https://doi.org/10.1038/s41596-020-00432-x
45. Villa JK, Amador P, Janovsky J, Bhuyan A, Saldanha R, Lamkin TJ, Contreras LM. 2017. A genome-wide search for ionizing-radiation-responsive elements in *Deinococcus radiodurans* reveals a regulatory role for the DNA gyrase subunit A gene's 5' untranslated region in the radiation and desiccation response. Appl Environ Microbiol 83:12. https://doi.org/10.1128/AEM.00039-17
46. Earl AM, Mohundro MM, Mian IS, Battista JR. 2002. The IrrE protein of *Deinococcus radiodurans* R1 is a novel regulator of *recA* expression. J Bacteriol 184:6216–6224. https://doi.org/10.1128/JB.184.22.6216-6224.2002
47. Blackwell GA, Hunt M, Malone KM, Lima L, Horesh G, Alako BTF, Thomson NR, Iqbal Z. 2021. Exploring bacterial diversity via a curated and searchable snapshot of archived DNA sequences. PLoS Biol 19:e3001421. https://doi.org/10.1371/journal.pbio.3001421
48. Eckweiler D, Dudek C-A, Hartlich J, Brötje D, Jahn D. 2018. PRODORIC2: the bacterial gene regulation database in 2018. Nucleic Acids Res 46:D320–D326. https://doi.org/10.1093/nar/gkx1091
49. Hyatt D, Chen G-L, Locascio PF, Land ML, Larimer FW, Hauser LJ. 2010. Prodigal: prokaryotic gene recognition and translation initiation site identification. BMC Bioinformatics 11:119. https://doi.org/10.1186/1471-2105-11-119
50. Mistry J, Chuguransky S, Williams L, Qureshi M, Salazar GA, Sonnhammer ELL, Tosatto SCE, Paladin L, Raj S, Richardson LJ, Finn RD, Bateman A. 2021. Pfam: the protein families database in 2021. Nucleic Acids Res 49:D412–D419. https://doi.org/10.1093/nar/gkaa913
51. Sweet P, Burroughs M, Jang S, Contreras L. 2023. TolRad: a model for predicting radiation tolerance using Pfam annotations identifies novel radiosensitive bacterial species from reference genomes and MAGs. bioRxiv. https://doi.org/10.1101/2023.11.02.562514
52. Cox MM, Keck JL, Battista JR. 2010. Rising from the ashes: DNA repair in *Deinococcus radiodurans*. PLoS Genet 6:e1000815. https://doi.org/10.1371/journal.pgen.1000815
53. Krisko A, Radman M. 2013. Biology of extreme radiation resistance: the way of *Deinococcus radiodurans*. Cold Spring Harb Perspect Biol 5:a012765. https://doi.org/10.1101/cshperspect.a012765
54. Minton KW. 1994. DNA repair in the extremely radioresistant bacterium *Deinococcus radiodurans*. Mol Microbiol 13:9–15. https://doi.org/10.1111/j.1365-2958.1994.tb00397.x
55. Minton KW, Daly MJ. 1995. A model for repair of radiation-induced DNA double-strand breaks in the extreme radiophile *Deinococcus radiodurans*. Bioessays 17:457–464. https://doi.org/10.1002/bies.950170514
56. Maslowska KH, Makiela-Dzbenska K, Fijalkowska IJ. 2019. The SOS system: a complex and tightly regulated response to DNA damage. Environ Mol Mutagen 60:368–384. https://doi.org/10.1002/em.22267
57. Liu F, Li N, Zhang Y. 2023. The radioresistant and survival mechanisms of *Deinococcus radiodurans*. Radiat Med Protect 4:70–79. https://doi.org/10.1016/j.radmp.2023.03.001
58. Bentchikou E, Servant P, Coste G, Sommer S. 2010. A major role of the RecFOR pathway in DNA double-strand-break repair through ESDSA in *Deinococcus radiodurans*. PLoS Genet 6:e1000774. https://doi.org/10.1371/journal.pgen.1000774
59. Slade D, Radman M. 2011. Oxidative stress resistance in *Deinococcus radiodurans*. Microbiol Mol Biol Rev 75:133–191. https://doi.org/10.1128/MMBR.00015-10
60. Weems AD, Welf ES, Driscoll MK, Zhou FY, Mazloom-Farsibaf H, Chang B-J, Murali VS, Gihana GM, Weiss BG, Chi J, Rajendran D, Dean KM, Fiolka R, Danuser G. 2023. Blebs promote cell survival by assembling oncogenic signalling hubs. Nature 615:517–525. https://doi.org/10.1038/s41586-023-05758-6
61. Zhou FY, Weems A, Gihana GM, Chen B, Chang B-J, Driscoll M, Danuser G. 2023. Surface-guided computing to analyze subcellular morphology and membrane-associated signals in 3D. arXiv. https://doi.org/10.48550/arXiv.2304.06176
62. Fackler OT, Grosse R. 2008. Grosse cell motility through plasma membrane blebbing. J Cell Biol 181:879–884. https://doi.org/10.1083/jcb.200802081
63. Coleman ML, Sahai EA, Yeo M, Bosch M, Dewar A, Olson MF. 2001. Membrane blebbing during apoptosis results from caspase-mediated activation of ROCK I. Nat Cell Biol 3:339–345. https://doi.org/10.1038/35070009
64. Esadze A, Stivers JT. 2018. Facilitated diffusion mechanisms in DNA base excision repair and transcriptional activation. Chem Rev 118:11298–11323. https://doi.org/10.1021/acs.chemrev.8b00513
65. Minsky A. 2003. Structural aspects of DNA repair: the role of restricted diffusion. Mol Microbiol 50:367–376. https://doi.org/10.1046/j.1365-2958.2003.03705.x
66. Tsai C-H, Liao R, Chou B, Palumbo M, Contreras LM. 2015. Genome-wide analyses in bacteria show small-RNA enrichment for long and conserved

intergenic regions. J Bacteriol 197:40–50. https://doi.org/10.1128/JB.02359-14
67. Schindelin J, Arganda-Carreras I, Frise E, Kaynig V, Longair M, Pietzsch T, Preibisch S, Rueden C, Saalfeld S, Schmid B, Tinevez J-Y, White DJ, Hartenstein V, Eliceiri K, Tomancak P, Cardona A. 2012. Fiji: an open-source platform for biological-image analysis. Nat Methods 9:676–682. https://doi.org/10.1038/nmeth.2019
68. Kluyver T, Ragan-Kelley B, Pérez F, Granger B, Bussonnier M, Frederic J, Kelley K, Hamrick J, Grout J, Corlay S, Ivanov P, Avila D, Abdalla S, Willing C, Jupyter Development Team. 2016. Jupyter Notebooks—a publishing format for reproducible computational workflows, p 87–90. IOS Press.
69. Perez F, Granger BE. 2007. IPython: a system for interactive scientific computing. Comput Sci Eng 9:21–29. https://doi.org/10.1109/MCSE.2007.53
70. McInnes L, Healy J, Saul N, Großberger L. 2018. UMAP: uniform manifold approximation and projection. J Open Source Softw 3:861. https://doi.org/10.21105/joss.00861